Microphysical properties of synoptic scale polar stratospheric clouds: In situ measurements of unexpectedly large HNO_3 containing particles in the Arctic vortex

Sergej Molleker[1], **Stephan Borrmann**[1,2], **Hans Schlager**[3], **Beiping Luo**[4], **Wiebke Frey**[1,*], **Marcus Klingebiel**[2], **Ralf Weigel**[2], **Martin Ebert**[5], **Valentin Mitev**[6], **Renaud Matthey**[7], **Wolfgang Woiwode**[8], **Hermann Oelhaf**[8], **Andreas Dörnbrack**[3], **Greta Stratmann**[3], **Jens-Uwe Grooß**[9], **Gebhard Günther**[9], **Bärbel Vogel**[9], **Rolf Müller**[9], **Martina Krämer**[9], **Jessica Meyer**[10], and **Francesco Cairo**[11]

[1]Max Planck Institute for Chemistry (MPI), Particle Chemistry Department, Mainz, Germany

[2]Institute for Physics of the Atmosphere (IPA), University of Mainz, Germany

[3]Deutsches Zentrum für Luft- und Raumfahrt (DLR), Institute of Atmospheric Physics, Oberpfaffenhofen, Germany

[4]Eidgenössische Technische Hochschule Zürich, Zürich, Switzerland

[5]Technical University Darmstadt, Darmstadt, Germany

[6]Centre Suisse d'Electronique et de Microtechnique SA (CSEM), Neuchâtel, Switzerland

[7]Laboratoire Temps-Fréquence, Institut de Physique, Université de Neuchâtel, Switzerland

[8]Institute for Meteorology and Climate Research, Karlsruhe Institute of Technology, Karlsruhe, Germany

[9]Institut für Energie- und Klimaforschung (IEK-7), Forschungszentrum Jülich GmbH, Jülich, Germany

[10]Institute of Energy and Environmental Technology e.V. (IUTA), Duisburg, Germany

[11]Institute of Atmospheric Science and Climate (ISAC-CNR), Rome, Italy

[*]Now at: School of Earth Sciences, The University of Melbourne, Melbourne, Victoria, Australia

Correspondence to: S. Borrmann (stephan.borrmann@mpic.de)

Abstract. In January 2010 and December 2011 synoptic scale PSC fields were probed during seven flights of the high altitude research aircraft M-55 *Geophysica* within the RECONCILE (Reconciliation of essential process parameters for an enhanced predictability of Arctic stratospheric ozone loss and its climate interaction) and the ESSenCe (ESSenCe: ESA Sounder Campaign) projects. Particle size distributions in a diameter range between 0.46 µm and 40 µm were recorded by four different optical in situ instruments. Three of these particle instruments are based on the detection of forward scattered light by single particles. The fourth instrument is a grey scale optical array imaging probe. Optical particle diameters of up to 35 µm were detected with particle number densities and total particle volumes exceeding previous Arctic measurements. Also, gas phase and particle bound NO_y were measured, as well as water vapor concentrations. The optical characteristics of the clouds were measured by the remote sensing lidar MAL (Miniature Aerosol Lidar) and by the in-situ backscattersonde MAS (Multiwavelength Aerosol Scatterometer), showing the synoptic scale of the encountered PSCs. The particle mode below 2 µm in size diameter has been identified as supercooled ternary solution droplets (STS). The PSC particles in the size range above 2 µm in diameter are considered to consist of nitric acid hydrates, and the particles' high HNO_3 content was confirmed by the NO_y instrument. Assuming a particle composition of nitric acid trihydrate (NAT), the optically measured size distributions result in particle-phase HNO_3 mixing ratios exceeding available stratospheric values. Therfore the measurement uncertainties concerning probable overestimations of measured particle sizes and volumes are discussed in detail. We hypothesize that either a strong asphericity or an alternate particle composition (e.g. water-ice coated with NAT) could explain our observations. In particular, with respect to the denitrification by sedimentation of large HNO_3-containing particles, generally considered as NAT, our new measurements raise questions concerning composition, shape and nucleation pathways. Answering these would improve the numerical simulation of PSC microphysical processes like cloud particle formation, growth, and denitrification, which

is necessary for better predictions of future polar ozone losses, especially under changing global climate conditions. Generally, it seems that the occurrence of large NAT particles -sometimes termed as NAT-rocks- are a regular feature of synoptic scale PSCs in the Arctic.

1   Introduction

The main role of polar stratospheric clouds (PSC) for the stratospheric ozone related chemistry can be divided into two major processes. These are the heterogeneous chlorine activation (Solomon et al., 1986; Solomon, 1999) and the redistribution of water and nitric acid due to sedimentation of cloud particles leading to dehydration and denitrification. The latter slows down chlorine deactivation through the formation of ClONO$_2$ in the polar spring. Denitrification can extend the ozone depleting season in the late spring, depending on the persistence of the polar vortex, ultimately resulting in lower stratospheric ozone values (Waibel et al., 1999). In the last decades, different types of PSC particles have been studied (see overviews in Peter and Grooß, 2011; Peter, 1997) and the ongoing research still aims to quantify their contributions to polar ozone chemistry as well as the microphysical mechanisms underlying their formation. The most frequent type of PSC particles are liquid aerosols: supercooled binary (SBS) or ternary solution (STS) droplets consisting of sulfuric acid, water and, in the case of a ternary solution, additionally nitric acid. These liquid particles likely dominate the chlorine activation (Solomon, 1999; Drdla and Müller, 2012; Wegner et al., 2012) in the Arctic and Antarctic. In particular the relative roles of SBS and STS in chlorine activation is still is a matter of scientific discussion. On the other hand, the major contribution to denitrification comes from solid nitric acid containing particles, which can grow to larger sizes leading to higher sedimentation speeds and efficient downward transport of nitrate compounds.

Solid nitric acid containing particles were suggested to exist in the form of hydrates (Crutzen and Arnold, 1986; Toon et al., 1986), although the nucleation processes of possible different hydrate types are not yet fully understood. Recent publications (Engel et al., 2013; Hoyle et al., 2013) show strong evidence for heterogeneous nucleation of solid PSC particles. A molar ratio of $3:1$ of water to nitric acid obtained in balloon-borne measurements (Voigt et al., 2000) confirms the existence of the most stable hydrate form – nitric acid trihydrate (NAT) – in the polar stratosphere. On the other hand, attempts to produce freely floating individual NAT particles in the lab failed so far, whereas nitric acid dihydrate (NAD) particles could be nucleated (Wagner et al., 2005, also in recent AIDA[1] measurements). The formation of metastable NAD seems to be favoured here compared to

NAT (Worsnop et al., 1993). Moreover, the nature of ice particles appears to be more complex as it also has been shown that a residual STS coating occurs during homogenous freezing of STS particles (Bogdan et al., 2010).

The particle measurements presented in this work were obtained mainly in the course of the RECONCILE field campaign in the winter 2009/2010 in Kiruna (67.8° N, 20.3° W). A comprehensive review of the RECONCILE campaign and the flight strategy of the Russian high altitude aircraft M-55 *Geophysica* is given in von Hobe et al. (2013). The first five of the 13 stratospheric flights occurred during the PSC season in the second half of January 2010. The minimum stratospheric temperatures in the polar vortex of the winter 2009/2010 were below the climatological mean (Dörnbrack et al., 2012) and low enough for formation of synoptic scale PSCs, which were widely observed by satellite lidar measurements (Pitts et al., 2011). The position of the polar vortex was shifted towards Europe (see Fig. 01) and moved over Sweden during the first part of the RECONCILE campaign. This aspect allowed long flight legs inside PSCs to be conducted. Two additional flights with a reduced instrumentation were performed from the same location in Kiruna (Sweden) in December 2011 during the ESSenCe campaign (Kaufmann et al., 2013). In analogy to Fig. 1 in Dörnbrack et al. (2012), for the temperature development in the Arctic stratosphere a similar graph provides here context for the two flights in December 2011 (Fig. 02). This plot shows that probing of PSCs occurred about a week after a relatively early and strong temperature drop at the beginning of December. The development of the temperature in the vortex before and during the ESSenCe flights at the 30 hPa level is illustrated in Fig. 03 with the two flight tracks drawn in panels of the corresponding dates. Although the flight altitude of the M-55 reached nearly 50 hPa, the temperature maps of the 30 hPa pressure level are shown because of the inherent assumption that large PSC particles must have nucleated at much higher altitudes and sedimented down from there. Regarding the structure of the polar vortex the temperature maps at 50 hPa, which are provided in the Supplement, look very similar, albeit shifted to somewhat higher temperature values.

As those cold synoptic conditions are relatively rare in the Arctic, previous in situ measurements have mostly documented mesoscale lee wave induced PSCs (Voigt et al., 2003; Lowe et al., 2006); only few reported PSC observations representative of synoptic conditions (Larsen et al., 2004; Weisser et al., 2006). The measurements reported here thus contribute to the investigation of PSC properties and particle formation on synoptic scales in the Arctic. Since there is a cooling trend in stratospheric temperatures (Randel et al., 2009; Thompson and Solomon, 2005; Ramaswamy et al., 2001) related to climate change the conditions for large scale PSC formation may be occurring more frequently in the future and the life times of PSCs may be extended. One particular focus of our study is the occurrence of extraordinar-

---

[1]AIDA (Aerosol, Interactions, and Dynamics in the Atmosphere) cloud chamber

ily large PSC particles in relatively high number densities. Here a mass-closure problem arises as the total NO$_y$ typically available within the polar vortex may not suffice to produce the corresponding large amounts of particle bound HNO$_3$.

2 Measurement techniques

Up to four different in situ optical particle instruments were deployed on the M-55 *Geophysica* aircraft. These were forward scattering spectrometer probes: FSSP-300 (Baumgardner et al., 1992, with the SPP-300 signal processing package upgrade from DMT Inc., Boulder, CO., USA; see also Sect. 3 in the Supplement), FSSP-100 (Dye and Baumgardner, 1984, also including an SPP-upgrade) and the CDP (Cloud Droplet Probe, Lance et al., 2010, from DMT Inc.). The fourth instrument was a grey scale optical array probe with a 15 μm pixel resolution (CIPgs, Cloud Imaging Probe from DMT Inc., e.g. Korolev, 2007). In this measurement technique (an optical array probe) a photo-diode line array is illuminated by the laser beam. While crossing the laser beam within a particle size dependent depth of field range, particles cast shadows by means of diffraction on the diode array. Consequently, the illumination of corresponding diodes is attenuated, whereby image data is recorded above one or multiple discrete attenuation/shadow thresholds. In our grey scale setup 35, 50 and 65 % shadow thresholds were used. The CIPgs probe was initially considered as having a lower size detection limit not suitable for PSC detection, nevertheless this probe collected useful data in low level clouds as well as inside PSCs. These four instruments had been modified for the deployment under the ambient conditions at high altitudes as encountered by the M-55 *Geophysica*. Additionally the data of the condensation particle counter (COPAS, Curtius et al., 2005; Weigel et al., 2009, here of the COPAS channel counting particles with diameter larger than 15 nm) were used in the presented results. COPAS has a maximum detectable particle diameter of a few μm, a limit given by the aspiration efficiency of the aerosol inlet.

2.1 Detection limits and sizing

Nominally the FSSP-300 can detect particle diameters down to 0.3 μm. Due to electronic noise consisting of multiple counts triggered by real particles, several (of the lower) size channels of the FSSP-300 had to be discarded from the data, which resulted in a higher size detection limit of 0.46 μm. This corrected limit was found by the correlation analysis between the five lowest FSSP-300 size channels and by a comparison with COPAS data, as the cloud particle number density reported by the FSSP-300 should not exceed the total aerosol number density detected by COPAS.

The size range of the deployed FSSP-100 was set to cover particle diameters from 1.05 to 37 μm. In particular the lower detection limit had to be corrected due to discrepancies found in the data when compared to the FSSP-300. This aspect of the FSSPs' intercomparison is described in the observations and results section.

The lower detection limit of the CDP should have been at a diameter of about 3 μm. However, due to instrumental problems related to extremely low ambient temperatures and insufficient heating during the CDP's first deployment in the stratosphere only in the last PSC-flight of the REC-ONCILE campaign particles larger than 7 μm were detected by the CDP. In the two ESSenCe flights two years later additional measures had been taken, the CDP performed well, and there its lower size detection limit was 4 μm. The upper size diameter limits of both FSSP instruments and of the CDP instrument were at 37 and 50 μm, respectively.

The sizing accuracy of the scattering probes (i.e. FSSP-100, FSSP-300, and CDP) is estimated to be about 10 % for spherical particles and correctly assumed refractive indices. However, the uncertainty is much higher in the regions with ambiguities in the Mie curve on which the sizing calibration is based. The bin limits of the FSSP probes were defined with the intention to fully contain ambiguities of the Mie curve, especially in the lower size range (i.e. 0.46–5 μm), to avoid false size classifications. The sizing calibration was calculated for the refractive index of NAT, with $n = 1.48$ taken as an average from the publications of Middlebrook et al. (1994) and Toon et al. (1990). The refractive index of STS ($n = 1.42$, depending on composition) is given in Krieger et al. (2000) and Luo et al. (1996). In the relevant particle diameter range below 1 μm the Mie curves for the refractive indices of STS and NAT are very close to each other with deviations of less than 10 % between them. The resulting size binning tables for the FSSPs are updated and adapted versions of those by Dye et al. (1992) and Borrmann et al. (2000).

2.2 Sample areas, number densities and counting statistics

The instruments' sample volumes for particle number density measurements were calculated as a product of the true air speed (from aircraft data) multiplied with the instrument-specific effective detection area, which is the so-called sample area. Values for the sample areas of the three forward scattering probes were measured by means of a newly designed calibration device in our laboratory similar to the one described by Lance et al. (2010). This was done before and after each campaign by scanning the instrument sample areas with a monodisperse droplet stream originating from a piezo-electric droplet generator. The following sample area values were used for the analysis of the PSC data: 0.09 mm^2 for FSSP-300, 0.42 mm^2 for FSSP-100, and 0.22 mm^2 for CDP. The respective uncertainties of these values are 10 % for the CDP and 15 % for the FSSPs.

With regard to the given sample areas one has to keep in mind that typical particle concentrations of PSCs result in very low counting statistics. While the STS mode and background aerosol was present with concentrations in the range of 1–$10\,\mathrm{cm}^{-3}$ (resolved only with FSSP-300), the concentrations of particles with diameters above 1–$2\,\mu\mathrm{m}$ lie in the range below $10^{-2}\,\mathrm{cm}^{-3}$ decreasing further for larger particles to below $10^{-3}\,\mathrm{cm}^{-3}$ at diameters above $10\,\mu\mathrm{m}$. The encounters of the FSSP-100 within long flight legs inside PSCs average to about 1 particle within $4\,\mathrm{s}$ corresponding to a flight distance of about $0.75\,\mathrm{km}$ between single detections. Consequently, time series for particle diameters above $2\,\mu\mathrm{m}$ were averaged over 100 to $200\,\mathrm{s}$. Averaging times of $500\,\mathrm{s}$ were used in the case of particle volume calculations where relatively large but rare particles contribute significantly. The counting statistics for the FSSP-300 are even lower, since its sample area is about a factor of 5 smaller than that of the FSSP-100.

2.3 Inter arrival time analyses

The complete removal of the data of the lowermost size channels of the FSSP-300 might have been avoided, if the instrument had the ability to record the precise time of each particle detection (i.e. electronic pulse). Multiple counts, electronic noise or other artifacts like detections of particles shattered on instrument parts can be identified and filtered based on shorter than expected interval times between these false detections.

The CDP instrument comprised such particle by particle data capability and allowed a so-called inter arrival times analysis. Figure 04 shows an example of the CDP measured distribution of inter arrival times (IAT) of PSC particles during the flight on 11 December 2011 suggesting a relatively homogeneous and random distribution of large PSC particles over a "spaghetti"-like sample volume of $0.22\,\mathrm{mm}^2$ cross section and $400\,\mathrm{km}$ length. Such analyses are usually less reliable with these instruments in the much smaller lee-wave PSCs. The homogeneity statement refers to scales larger than a mean average distance of about $1\,\mathrm{km}$ between particle detections. Nevertheless, this distribution does not show significant variations in the number density, which would be expected in a lee wave induced PSC field. Based on such distributions measurement artifacts like shattering or electronic noise could have been identified by increased numbers of short particle inter arrival times. Unlike for other measurements in cirrus (e.g., de Reus et al., 2009; Frey et al., 2011) shattering artifacts were not found in the PSC data considered here. Although the FSSPs lacked the particle by particle data record, the low numbers of counts per second in PSCs (referring to $\mathrm{D} > 2\,\mu\mathrm{m}$) made a similar, but coarser analysis possible. The fraction of one second (i.e. instrument's integration interval) values with more than one count agreed to the estimated low probability for an average count rate of one particle in a few seconds based on Poisson statistics.

Consequently, artifacts were not found in this data as well. Also, shattering usually is associated with much larger particle sizes (i.e. $> 100\,\mu\mathrm{m}$ in diameter) for these instrument geometries.

2.4 Further instrumentation

Reactive Nitrogen (NO$_y$) instrument: the optical particle measurements were juxtaposed with data from the NO$_y$ instrument SIOUX (Voigt et al., 2005), which was sampling with one forward and one rear facing inlet measuring total and gas phase NO$_y$, respectively. The total NO$_y$ signal was capable of resolving individual HNO$_3$ containing particles with sizes greater than $5\,\mu\mathrm{m}$ and ambient number densities smaller than $4 \times 10^{-4}\,\mathrm{cm}^{-3}$ as single peaks in the $1\,\mathrm{Hz}$ signal data time series. Here, we use only the detected individual NO$_y$ containing particles which were analyzed according to the single particle detection method as described by Northway et al. (2002).

Aerosol Backscatter sonde: the bulk optical properties of the particle population were detected by the aerosol backscatter sonde MAS (Cairo et al., 2004). The instrument is basically a near range lidar that probes the atmosphere from 3 to $100\,\mathrm{m}$ from the aircraft. It fires a $532\,\mathrm{nm}$, $1\,\mathrm{ns}$ laser pulse and detects the light return from air molecules and aerosol particles resolved in two polarization channels. The instrument thus delivers aerosol volume backscatter coefficients and depolarization profiles with a time resolution of $5\,\mathrm{s}$ and a spatial resolution of $25\,\mathrm{cm}$ perpendicular to the aircraft's flight path. In this study we only report aerosol depolarization values computed for aerosol backscatter ratio (ratio of the aerosol to molecular volume backscatter coefficients) greater than 1, as above that value we can provide absolute uncertainties below $5\,\%$.

Miniature Airborne Lidar (MAL): the range-resolved backscatter and depolarization profiles are obtained with two independently operating standalone lidar instruments installed on the aircraft, referred to respectively as MAL1 (probing in upward direction) and MAL2 (probing in downward direction; Mitev et al., 2002). The lidars use a Nd : YAG pulsed laser at a wavelength of $532\,\mathrm{nm}$. The altitude- and time-resolution of the signal acquisition is about $20\,\mathrm{m}$ and $6\,\mathrm{s}$, respectively, but in the data processing the resolutions are degraded, in order to achieve adequate signal-to-noise ratio. An intercomparison of the total backscatter and depolarization backscatter coefficients measured by the two MALs and the CALIPSO-CALIOP lidar (Pitts et al., 2011) was also performed during RECONCILE campaign (Mitev et al., 2012). Further details on MAS and MAL instruments can be found in Sect. 4 of the supplementary material.

Water Vapor: a Hygrometer based on Lyman-alpha fluorescence technique (FISH, Fast In situ Stratospheric Hygrometer; Zöger et al., 1999) was deployed on the aircraft. Here water vapor mixing ratios are used for the calculation of the frost point and the equilibrium temperature of NAT.

Air temperature: the ambient temperature measurements with an accuracy of 0.5 K (only RECONCILE) were provided by an instrument called TDC (Thermo Dynamic Complex; Shur et al., 2007). During ESSenCe a different temperature instrument (aircraft data) had to be adopted with higher uncertainty of $+0.5/-1.5$ K.

MIPAS-STR: Volume mixing ratios of various trace gas species, temperature and cloud parameters were derived from the MIPAS-STR (Michelson Interferometer for Passive Atmospheric Sounding – STRatospheric aircraft) passive infrared limb observations (Woiwode et al., 2012, and references therein). Here HNO₃ profiles obtained during the RECONCILE season are used for comparison with the in situ data.

3 Observations and results

In total, about 13 flight hours distributed over seven flights were spent inside PSCs. The data availability of the various instruments for these flights is shown in the Table S1 in the supplement. Continuous PSC fields in flight legs of more than one hour corresponding to about 700–900 km illustrate the synoptic scale character of PSCs in both winters. Figure 05 shows a MAL profile with a flight leg inside a 900 km long PSC field of the flight on 20 January 2010. Time series for three flights (Fig. 06) show number concentrations mostly derived from FSSP measurements together with temperatures relevant for PSC existence. For the calculation of the NAT equilibrium temperature T_{NAT} (Hanson and Mauersberger, 1988) water vapor concentration measurements of the FISH instrument and NO$_y$ data of the SIOUX instrument were used, with an assumed fraction of HNO₃ in NO$_y$ of 75 % (Wetzel et al., 2012). In the absence of NO$_y$ data, the values of 5 and 10 ppbv were used as upper and lower estimates. For the calculation of the ice equilibrium temperature (frost point, T_{ICE}) the parameterization of Marti and Mauersberger (1993) and the FISH data were applied. Most of the PSC measurements were obtained at flight altitudes of about 18 km, with a maximum just below 19 km and lowest altitudes at 16.8 km. Thus, our investigations are limited to the lower altitude levels of typical PSC occurrence.

The number density measured by the FSSP-300 shows an anti-correlation with temperature (Fig. 06a) and reaches the values measured by COPAS at the lowest temperatures of about 188 K. For events like these it can be assumed that the background aerosol was almost completely activated to cloud particles, which implies that these particles grow to sizes above the FSSP's lower detection threshold. The COPAS count levels were in the 6–14 particles cm^{-3} range and thus the COPAS instrument provides an upper limit for the maximum concentration that can possibly be detected by the FSSP-300. The FSSP-300s total number density did not exceed COPAS values, as evident from Fig. 06a.

Instruments like the CDP and FSSP have a small cross-sectional area within the laser beam intensity profile. Particles passing through this "window" are accepted for (accurate) sizing. For this a technique based on a depth of field (DoF) criterion is used, which results in the rejection of out-of-focus particles from the size measurement. Nevertheless, they are detected and counted into a separate data channel, albeit without size information. In essence, the size distribution is determined by analyzing only a subset of the total number of particles seen by the instrument. The typical ratio of Depth of Field rejected to accepted particles (DoF ratio) of the CDP could be used to validate the FSSP-100 measurements by deriving the concentration from the CDP time series records of DoF rejected particles. The relatively high DoF ratio leads to much lower statistical uncertainty of the resulting time series. Although the DoF number counts and the DoF ratio depend on particle size, the confined detection range of the CDP (hier above 7 μm) and the limited size range of PSC particles (mostly below 20 μm) allowed to estimate a fixed DoF ratio valid for this size range between 7 and 20 μm. The constant value for the fixed DoF ratio was obtained from different measurements in low level Arctic clouds, where narrow quasi-monomodal size distributions with modal peaks between 12 and 22 μm (i.e. close to the sizes of the PSC particles) were encountered. The result for a DoF ratio of 20 is illustrated in Fig. 06b, where the corresponding FSSP-100 concentration for diameters above 4.7 μm is in a very good agreement with the CDPs DoF rejected counts.

For the same RECONCILE flight as in Fig. 06b a PSC size distribution is illustrated in Fig. 07 which shows a good agreement between both instruments. Similarly, the time series of the FSSP-100 and CDP measurements displayed in Fig. 06c from the ESSenCe flight agree well.

Where data from the FSSP-300 are available two distinct particle modes can be observed in the size distributions. In most of the measured size distributions the particle number density spans 2–3 orders of magnitude over a size diameter range from 1 to 2 μm (Fig. 08), which also can be seen from the time series of different sizes in Fig. 06a.

The simultaneous measurement of the two FSSPs of different lower size detection limits showed a discrepancy in the particle concentration of 1–2 orders of magnitude in the overlapping size bin between 0.8 and 2 μm (Fig. 08). In this region, a steep slope in the measured particle size distribution coincides with the ambiguity of the Mie calibration curve and a decreasing sensitivity of the FSSP-100. As a consequence, the lower detection limit of the FSSP-100 was corrected from the initial 0.8 to 1.05 μm, such that good agreement between both FSSPs for sizes from 1.05 to 2 μm was reached.

Additionally, in some time intervals the particle concentration in the size interval from 2 to 5 μm is lower than in the size range above, indicating a separation of the two particle modes. Clearly, owing to fast sedimentation (about 1.7 cm s^{-1} or 61 m/hour for a NAT particle of 14 μm in diameter),

the particles from the upper and lower size modes originate from different air masses.

3.1   Ternary solution droplet mode

The interpretation of the sub-micron particle mode, which was partly resolved by the FSSP-300 measurement (Fig. 08) as the STS-mode, can be tested by its particle volume vs. temperature dependence. The dependence of particle volume on ambient temperature in PSCs consisting of STS is driven by the increased uptake of water and HNO$_3$ with decreasing temperature. The particulate volumes were calculated from the measured number size distributions and plotted as a function of temperature (as discussed in Peter, 1997). Also included are STS-mode volumes derived from theory based on STS thermodynamics following Carslaw et al. (1995). The theoretical volumes of the STS particle mode shown as solid black lines in Fig. 09 were calculated accounting for the FSSP-300's detection limit – in our study at 0.46 μm –, which differs from the limits of this instrument used by Dye et al. (1992), and Peter (1997). Four theoretical curves representing STS with different values for assumed total available HNO$_3$ mixing ratios of 2, 5, 10 and 15 ppbv are shown. With the intent to exclude the NAT phase the particle volumes were evaluated from the FSSP-300 size distributions only including diameters less than 2 μm (points marked as crosses) while particles with larger sizes (also present in the same size distributions) were excluded from the volume determination. The STS particulate volumes calculated in this way show a reasonably good agreement with the theoretical particle volume dependence of STS. The time intervals considered here were selected from parts of the flight track experiencing a wider temperature range, which for given flight profiles implied that the aircraft did not stay on a constant potential temperature altitude level (but rather within an altitude range of up to 1.5 km). Therefore, the airmass content of trace gases, in particular of HNO$_3$ is not expected to be constant. Also the calculation of volume curves for STS does not account for possible partitioning of HNO$_3$ into larger solid particles (e.g. NAT) which were always present in these measurements.

The finding that STS particles were present in large number densities is corroborated by the lidar measurements shown in Fig. 010 where a scatterplot of aerosol depolarization vs. backscatter ratio is reported. Here the lidar MAL (red crosses; see also the supplement Sect. 4) and the near-range backscatter sonde MAS probed the same 20 January PSC (black crosses) as shown in Fig. 05. Also PSC data from 17 January (green squares) and 25 January 2010 (blue squares) are included in Fig. 010. While the latter showed depolarization around 9 %, indicating a detectable presence of solid/aspherical particles, the former two displayed no significant aerosol depolarization, confirming that the STS particle contribution to the optical characteristic of these clouds was dominant. Nevertheless, some signal in the depolariza-

tion channel is still present and indicates that solid particles, probably NAT, with number densities much below those of the STS droplets, always were present embedded in the predominant STS clouds. The temperature dependence of the STS-Mode corresponds well to the strong anti-correlation of the FSSP-300 number concentration with temperature. The time series of the number concentration from the FSSP-300 in Fig. 06a can be interpreted as the varying fraction of the STS-mode above the instrument's detection limit of 0.46 μm. At the lower temperatures of about 187 K the FSSP-300 measured almost the same particle number density as the CO-PAS instrument in the channel for particles larger than 15 nm. At slightly higher temperatures the STS droplets right at the lower detection limit of the FSSP-300 may be just about too small to be detected by the instrument. Thus with changing temperature STS droplets smaller than 0.46 μm may "grow into or shrink out of" the detection limit window of the FSSP-300. This behavior also is illustrated for size distributions measured in air of different ambient temperatures (Fig. 011), where the difference is discernible in the FSSP-300 data and in the first one to two bins (e.g. Dp below 1.9 to 3.3 μm) of the FSSP-100 data.

3.2   NAT and the large particle mode

Throughout all PSC-flights particles above 2 to 3 μm in diameter were frequently detected by the FSSP instruments, in some flights reaching number concentrations of up to 0.8×10^{-2} cm^{-3} (Fig. 06c).

Considering that the in situ recorded ambient temperatures mostly were 2–5 K above the frost point but still below T_{NAT}, the assumption that these larger particles consist of NAT seems plausible (Dye et al., 1992). The volume of the particle phase evaluated for diameters above 2 μm is also included in the volume vs. temperature graph of Fig. 09 as filled symbols. Many of these data points for volume fall into an area near the schematically drawn dashed line for NAT. These data points were calculated using 500 s flight intervals to reduce errors due to counting statistics. Furthermore, it can be seen from the figure that some data points of the ESSenCe measurements were recorded above the NAT equilibrium temperature (T_{NAT}), and hence the particles were in a non-equilibrium state, that is they were evaporating. On the other hand, ambient temperature was measured with higher uncertainty during ESSenCe flights (+0.5/−1.5 K) compared to the accuracy of the TDC used throughout REC-ONCILE. Therefore, a data point with 2 K above T_{NAT} in the ESSenCe campaign might be partly attributed to a positive bias in the temperature measurement.

Maximum values of particle volume, arising from the part of the particle size distribution with diameters above 2 μm, correspond to distributions with shapes as those depicted in Fig. 011 and Fig. 012. It is worthwhile noting that these distributions represent particle volumes slightly (as in the left panel of Fig. 012) or significantly (as in the right panel of

Fig. 012 for the 11 December 2011 ESSenCe flight) bigger than what was reported from other Arctic measurements (for instance Brooks et al., 2003; Fahey et al., 2001). In particular, during the ESSenCe flight the observed volume of the particle phase was twice as large as previously reported. The main contribution to the particle volume results from particles with diameters close to the mode maximum at 12 to 15 µm (e.g. in Fig. 012). Unfortunately, the NO_y instrument was not deployed during the ESSenCe flights.

For RECONCILE evidence that the large particles contain HNO_3 is provided by the NO_y-instrument SIOUX, which detected a high amount of HNO_3 in the particle phase. No instrumentation to measure the molar ratio with respect to water in the particles was available. Partly due to a large enhancement factors F for particles with diameters above 10 µm (with F roughly between 10 to 18) and the relatively high overall particle number density the total NO_y signal of the SIOUX instrument went into saturation in time intervals when the most noticeable FSSP size distributions were obtained. Examples for these time intervals are shown in Figs. 07 and 011 (right panel). For two time intervals with particle concentrations below $0.002\,\mathrm{cm}^{-3}$ and where the NO_y instrument was not saturated two size distributions have been retrieved (see Fig. 013) from the NO_y data by the single particle detection method as described in Northway et al. (2002). Particle sizes were calculated assuming spherical shapes and a NAT composition. The sensitivity of the method scales with particle volume, resulting in a lower detection size diameter limit of 5 µm. The discrepancy between the values obtained with NO_y and optical particle detection seems to repeat the findings of Brooks et al. (2003) (optical) and Fahey et al. (2001) (NO_y), where the optically detected particle number densities exceeded those obtained from the NO_y signal as well. Additionally, such discrepancies are compatible with the assumption of aspherical particle shapes, because in these cases the real enhancement factor of the NO_y inlet would be lower, especially for smaller particles.

Despite such uncertainties in the number density and the discrepancy with the optically measured size distribution, the NO_y retrieval provides trustworthy volume equivalent sizes for the assumed NAT composition of up to 20–24 µm particle diameter – keeping in mind that only unsaturated time intervals were evaluated. The uncertainty of the individual particle size calculation assuming NAT is estimated to be 20 %.

Additional support for the presence of large PSC particles comes from the CIPgs image data. Although optical array probes are designed mainly for measuring sizes and shapes of ice crystals larger than roughly 50 to 100 µm, the CIP grey scale with a pixel resolution of 15 µm collected data in PSCs just at its lowermost detection limit. A maximum of 149 images were detected in one flight (25 January 2010) over a flight distance of 1200 km. The image buffer from a 30 minute interval of the same flight is illustrated in Fig. 014. The numbers of such 2 to 6 pixel images recorded by the CIPgs are given in Table 1, where these numbers are compared to numbers of FSSP-detections above two particle diameter thresholds, 15 and 20 µm. The particle numbers determined by the two independent instruments and different measurement techniques seem to correlate. The estimated sample area of the CIPgs instrument for a 15 µm particle diameter is about $0.5\,\mathrm{mm}^2$, which is slightly larger but close to that of the FSSP-100 with its value of $0.42\,\mathrm{mm}^2$. We consider these triggered pixels as first quasi-visual evidence for the existence of large NAT rock type particles. A short note on chemical analyses of the non-volatile aerosol particles collected with an impactor technique is provided in the supplementary material, Sect. 2.

4   Discussion and open questions

Assuming that the particles detected by the FSSP instruments are composed solely of NAT, the measured particulate volumes can be expressed in terms of HNO_3 equivalent mixing ratios. Such HNO_3 mixing ratios (from the particle phase only) were calculated using data averaged over 500 s and resulted in maximum values of up to 17 ppbv±40 % (January 2010) and up to 25–35 ppbv±40 % (11 December 2011). To put these numbers into perspective some of the total HNO_3 (particle plus gas phase) mixing ratios were included in Fig. 015, which shows HNO_3-profiles obtained by the infrared limb-sounder MIPAS-STR deployed on the same aircraft. The vertical resolution of the shown retrieval results is about 1 km. A maximum for the re-nitrification of about 9 ppbv (from 7 to 16 ppbv) was found at 405 K potential temperature altitude on 30 January, i.e. at the end of the PSC season during RECONCILE.

At this point it is uncertain, how much overestimation of particle-derived HNO_3 can be explained by the large spatial averaging of the remote sensing instrument, although the in situ particle data have been averaged over long spatial intervals too (about 90 km). Different air volumes are observed by MIPAS-STR and the in situ instruments because the MIPAS-STR limb observations integrate radiation along the viewing direction approximately perpendicular to the flight track with the largest contributions arising from the region around the tangent points of the observations. These are between a few tens to few hundreds of kilometers away from the flight path of the *Geophysica* depending on the tangent altitude. The in situ gas-phase-NO_y measurement showed maximum values of 10 to 14 ppbv HNO_3 at the potential temperature levels corresponding to the renitrified layer (24–25 January 2010). The Chemical Lagrangian Model of the Stratosphere (CLaMS) yields maximum values of 16–17 ppbv for the total HNO_3 (Grooß et al., 2014). Contrary to that, the particle volume detected on 11 December 2011 corresponds to mixing ratios of 25–35 ppbv (±40 %) of HNO_3. Therefore, questions about the assumed NAT composition arise, as such

values exceed any measured HNO$_3$ mixing ratio in the Arctic stratosphere.

Besides the high particle volume or HNO$_3$ content, NAT particle sizes above 10 µm in diameter are increasingly constrained by the available growth time and related sedimentation times and altitudes. A backward model calculation starting from the PSC field of the flight track on 11 December 2011 can accommodate a NAT particle of only up to 16 µm, where already by 20 % increased growth rate and by 10 % reduced sedimentation speed were assumed in the model (LAGRANTO trajectories based on ERA-Interim data were used here). Similar results by Fahey et al. (2001) showed that only particles of up to 16–18 µm in diameter (so called "NAT-Rocks") exhibit realistic back trajectories, whereby it took these particles up to 4 to 6 days to grow to such sizes. Contrary to such theoretical considerations our FSSP size distributions from inside synoptic scale PSCs extend to optical particle diameters of up to 35 µm (Figs. 07 and 012), although only very few particles of diameters larger than 24 µm were recorded.

In Fig. 012 also model simulations for size distributions are shown. These were created by CLaMS Model, which includes a NAT particle scheme (Grooß et al., 2014; Kaufmann et al., 2014). The NAT particles were nucleated using a saturation-dependent nucleation scheme (Hoyle et al., 2013). Particle growth, evaporation and sedimentation were calculated along trajectories for the individual so-called particle parcels. For the comparison with the observations, all particle parcels within 100 km of the chosen flight path segment were taken into account. As also can be seen for another flight on 22 January 2010 (Grooß et al., 2014) the simulated NAT size distribution peaks in the same order of magnitude as do the observations, although NAT particles with diameters larger than 10 um are not reproduced by the model.

The FSSP-derived diameters for spherical particles combined with an assumption of a pure NAT composition seem to overestimate HNO$_3$ content in the condensed phase. Moreover, microphysical model simulations coupled to computed sedimentation speeds fail to reproduce the largest observed particles. Two hypotheses or a combination of both can help resolving such discrepancies: (a) strong asphericity of NAT particles, affecting both sedimentation and optical sizing and (b) an additional particle type consisting of a NAT layers on ice-particles, as suggested earlier by Peter et al. (1994).

4.1 Hypothesis 1: aspherical large NAT particles

There is still a lack of direct measurements of the morphology of large HNO$_3$-containing PSC particles since most laboratory experiments for example concerning their heterogeneous chemical reactivity had been carried out with NAT deposits on substrates. Thus, one can only be speculate about the precise airborne particle shapes. In Woiwode et al. (2014) reduced NAT particle settling velocities as a consequence of potentially non-compact or non-spherical NAT particles are assumed to simulate the vertical redistribution of HNO$_3$. The comparison of simulated and observed gas-phase HNO$_3$ is consistent with moderately reduced settling velocities relative to compact spherical particles. Moderately reduced settling velocities would e.g. be expected for compact significantly elongated particles.

It is clear that the degree of asphericity affects the size calibration of the FSSP. In Borrmann et al. (2000) moderate asphericities of up to 1 : 2 were tested for the FSSP configuration using the T-matrix method. The result is that the scattering cross section averaged over all orientations is still close to the Mie calculation. On the other hand, the asphericity would broaden the resulting FSSP size distribution, of which the oversized part would contribute stronger to the particle volume. To test the maximum contribution of this effect the size distribution can be reduced to one size bin of the maximum particle count. For the size distribution of maximum particle volume (11 December 2011, Fig. 012, right panel) such a hypothetical maximum broadening would increase the total particulate volume only by 21 %. In addition, the unexpected maximum particle sizes above 20 µm in diameter are rather rare and contribute not more than 20 % to the total particle volume despite their large individual sizes. Obviously, the particle volume is very sensitive to the measured particle size and further errors due to asphericity higher than 1 : 2 are possible. Inaccurate density and refractive index assumptions might contribute as well to the size error and the overestimated particulate volume. By comparison, NAD dihydrate particles nucleated within the AIDA chamber (Wagner et al., 2005) were best explained by oblate particles with asphericities (ratio of the rotational to horizontal axes) of about 1 : 5.

4.2 Hypothesis 2: NAT-coated-ice

The second hypothesis is based on NAT layers growing on preexisting ice particles. CALIOP satellite measurements of the winter 2009/2010 show frequent ice observations (Pitts et al., 2011). For the winter 2011/2012 the temperature in the polar vortex was close to the frostpoint about one day before the measurement flight on 11 December 2011 (Fig. 02). A simple test by analyzing back trajectories (HYSPLIT[2]) results in temperatures close to the frost point over Greenland about 20 h prior to the in situ measurements. For this it was assumed that a sedimentation speed of 100 m h^{-1} or 2.8 cm s^{-1} corresponds to particle diameters of about 18 µm for NAT or 25 µm for ice density (Müller and Peter, 1992). It is conceivable that lee waves over Greenland resulted in even lower temperatures than resolved in the models, this way providing conditions where ice particles might have grown within minutes to significant sizes. If such particles later acquire a NAT coating with the ice evaporating when ambient temperatures rise above the frost point, then hollow NAT

---

[2]HYSPLIT – Hybrid Single Particle Lagrangian Integrated Trajectory Model, NOAA

shells may result which have large (optical) sizes but lower HNO$_3$ mass than solid NAT particles of the same size. Moreover, many back trajectories (also from the RECONCILE campaign) starting from in situ measurement points lead to ambient temperatures above T_{NAT} within about 48 h prior to the measurement, which gives a pure and compact NAT particle not enough time to grow to the detected large particle diameters. A publication of Goodman et al. (1997) based on Antarctic in situ measurements shows impactor replicas of presumably ice particles with sizes of up to 30 μm, although the replicas where collected at ambient temperature of 2–3 K above the frost point. The technique used there indicated also the presence of NO$_3^-$ ions in these particles, which supports the hypothesis of a NAT layer on ice. Moreover, laboratory measurements initially conceived to prove that NAT coated ice particles can survive for some time under ambient temperatures above the frost point because of such "protective NAT coating" showed the opposite, namely, that the NAT layer does not prevent the underlying ice substrate from evaporation (Biermann et al., 1998; Peter et al., 1994). For these reasons the hypothesis of left over hollow NAT shells with large optical cross sections after the evaporation of underlying ice seems viable. Future specialized laboratory experiments should be dedicated to the exploration of this possibility.

5   Summary and conclusions

A comprehensive data set of optical in situ measurements of PSCs was obtained in two Arctic winter vortices. Cloud particles were detected on synoptic scales mostly below T_{NAT} but above ice saturation temperature. The prevailing type of detected size distribution was a mixture of the submicron sized STS and a large particle mode (around 15 μm diameter) with high HNO$_3$ content. The assumption of solid compact NAT particles leads to the following discrepancies: the amount of the resulting condensed HNO$_3$ exceeds stratospheric values, and particles settling velocities and growth times can not be reconciled with back trajectories. Maximum particle sizes derived from the NO$_y$-measurements are still well above the limits obtained from trajectory calculations. It is hypothesized that such discrepancies can be resolved if particles are strongly aspherical or the composition of the largest particles, at least at a certain stage of their formation is not pure NAT, e.g. NAT coated ice or NAT shells grown on ice. Similar as for measurements by Brooks et al. (2003) and Fahey et al. (2001), the FSSP (optically) detected particle number density outnumbers the concentrations inferred from the NO$_y$ measurements. This behavior is to be expected, if the calculation of the enhancement factor of the NO$_y$ sampling inlet did not account for large asphericity of the particles having higher aerodynamic diameters. Beyond the proposed hypotheses this work cannot clarify the precise nature of the large HNO$_3$ containing particles. Both solutions might

be possible, because it has also been shown, that NAT particles nucleate without preexisting ice particles (Voigt et al., 2003), though this publication reports particle diameters only of up to 8 μm.

Large particles introduced as "NAT rocks" seem to frequently occur in synoptic scale PSCs of which a substantial set of particle size distributions was collected. For the first time this particle type was detected with an optical array probe. Direct measurements of the morphology of PSC particles are highly desirable and will enable an appropriate size calibration of the FSSP for refining and possibly re-visiting the measurements presented in this and previous studies. As the stratospheric temperatures are decreasing in connection with climate change, synoptic scale PSCs may form more wide spread, more frequently and with longer life times in the future. Besides the chemical effects of PSCs their influence on the local and regional radiative budgets may also become increasingly relevant. For these reasons detailed studies on the properties of PSCs continue to be important for atmospheric science.

References

Baumgardner, D., Dye, J. E., Gandrud, B. W., and Knollenberg, R. G.: Interpretation of measurements made by the forward scattering spectrometer probe (FSSP-300) during the Airborne Arctic Stratospheric Expedition, Journal of Geophysical Research: Atmospheres, 97, 8035–8046, http://dx.doi.org/10.1029/91JD02728, 1992.

Biermann, U. M., Crowley, J. N., Huthwelker, T., Moortgat, G. K., Crutzen, P. J., and Peter, T.: FTIR studies on lifetime prolongation of stratospheric ice particles due to NAT coating, Geophysical Research Letters, 25, 3939–3942, http://dx.doi.org/10.1029/1998GL900040, 1998.

Bogdan, A., Molina, M. J., Tenhu, H., Mayer, E., and Loerting, T.: Formation of mixed-phase particles during the freezing of polar stratospheric ice clouds, Nat. Chem., 2, 197–201, http://dx.doi.org/10.1038/nchem.540, 2010.

Borrmann, S., Luo, B., and Mishchenko, M.: Application of the T-matrix method to the measurement of aspherical (ellipsoidal) particles with forward scattering optical particle counters, Journal of Aerosol Science, 31, 789–799, http://dx.doi.org/10.1016/S0021-8502(99)00563-7, 2000.

Brooks, S. D., Baumgardner, D., Gandrud, B., Dye, J. E., Northway, M. J., Fahey, D. W., Bui, T. P., Toon, O. B., and Tolbert, M. A.: Measurements of large stratospheric particles in the Arctic polar vortex, J. Geophys. Res., 108, D20, http://dx.doi.org/10.1029/2002JD003278, 2003.

Cairo, F., Adriani, A., Viterbini, M., Di Donfrancesco, G., Mitev, V., Matthey, R., Bastiano, M., Redaelli, G., Dragani, R., Ferretti, R., Rizi, V., Paolucci, T., Bernardini, L., Cacciani, M., Pace, G., and Fiocco, G.: Polar stratospheric clouds observed during the Airborne Polar Experiment - Geophysica Aircraft in Antarctica (APE-GAIA) campaign, Journal of Geophysical Research: Atmospheres, 109, D07204, http://dx.doi.org/10.1029/2003JD003930, 2004.

Carslaw, K. S., Luo, B., and Peter, T.: An analytic expression for the composition of aqueous HNO$_3$-H$_2$SO$_4$ stratospheric aerosols including gas phase removal of HNO$_3$, Geophysical Research Letters, 22, 1877–1880, http://dx.doi.org/10.1029/95GL01668, 1995.

Crutzen, P. J. and Arnold, F.: Nitric acid cloud formation in the cold Antarctic stratosphere: a major cause for the springtime 'ozone hole', Nature, 324, 651–655, http://dx.doi.org/10.1038/324651a0, 1986.

Curtius, J., Weigel, R., Vössing, H.-J., Wernli, H., Werner, A., Volk, C.-M., Konopka, P., Krebsbach, M., Schiller, C., Roiger, A., Schlager, H., Dreiling, V., and Borrmann, S.: Observations of meteoric material and implications for aerosol nucleation in the winter Arctic lower stratosphere derived from in situ particle measurements, Atmospheric Chemistry and Physics, 5, 3053–3069, http://dx.doi.org/10.5194/acp-5-3053-2005, 2005.

de Reus, M., Borrmann, S., Bansemer, A., Heymsfield, A. J., Weigel, R., Schiller, C., Mitev, V., Frey, W., Kunkel, D., Kürten, A., Curtius, J., Sitnikov, N. M., Ulanovsky, A., and Ravegnani, F.: Evidence for ice particles in the tropical stratosphere from in-situ measurements, Atmospheric Chemistry and Physics, 9, 6775–6792, http://dx.doi.org/10.5194/acp-9-6775-2009, 2009.

Dörnbrack, A., Pitts, M. C., Poole, L. R., Orsolini, Y. J., Nishii, K., and Nakamura, H.: The 2009–2010 Arctic stratospheric winter – general evolution, mountain waves and predictability of an operational weather forecast model, Atmospheric Chemistry and Physics, 12, 3659–3675, http://dx.doi.org/10.5194/acp-12-3659-2012, 2012.

Drdla, K. and Müller, R.: Temperature thresholds for chlorine activation and ozone loss in the polar stratosphere, Annales Geophysicae, 30, 1055–1073, http://dx.doi.org/10.5194/angeo-30-1055-2012, 2012.

Dye, J. E. and Baumgardner, D.: Evaluation of the Forward Scattering Spectrometer Probe. Part I: Electronic and Optical Studies, J. Atmos. Oceanic Technol., 1, 329–344, http://dx.doi.org/10.1175/1520-0426(1984)001⟨0329:EOTFSS⟩2.0.CO;2, 1984.

Dye, J. E., Baumgardner, D., Gandrud, B. W., Kawa, S. R., Kelly, K. K., Loewenstein, M., Ferry, G. V., Chan, K. R., and Gary, B. L.: Particle size distributions in Arctic polar stratospheric clouds, growth and freezing of sulfuric acid droplets, and implications for cloud formation, Journal of Geophysical Research: Atmospheres, 97, 8015–8034, http://dx.doi.org/10.1029/91JD02740, 1992.

Engel, I., Luo, B. P., Pitts, M. C., Poole, L. R., Hoyle, C. R., Grooß, J.-U., Dörnbrack, A., and Peter, T.: Heterogeneous formation of polar stratospheric clouds – Part 2: Nucleation of ice on synoptic scales, Atmospheric Chemistry and Physics, 13, 10 769–10 785, http://dx.doi.org/10.5194/acp-13-10769-2013, 2013.

Fahey, D. W., Gao, R. S., Carslaw, K. S., Kettleborough, J., Popp, P. J., Northway, M. J., Holecek, J. C., Ciciora, S. C., McLaughlin, R. J., Thompson, T. L., Winkler, R. H., Baumgardner, D. G., Gandrud, B., Wennberg, P. O., Dhaniyala, S., McKinney, K., Peter, T., Salawitch, R. J., Bui, T. P., Elkins, J. W., Webster, C. R., Atlas, E. L., Jost, H., Wilson, J. C., Herman, R. L., Kleinböhl, A., and von König, M.: The Detection of Large HNO$_3$-Containing Particles in the Winter Arctic Stratosphere, Science, 291, 1026–1031, http://dx.doi.org/10.1126/science.1057265, 2001.

Frey, W., Borrmann, S., Kunkel, D., Weigel, R., de Reus, M., Schlager, H., Roiger, A., Voigt, C., Hoor, P., Curtius, J., Krämer, M., Schiller, C., Volk, C. M., Homan, C. D., Fierli, F., Di Donfrancesco, G., Ulanovsky, A., Ravegnani, F., Sitnikov, N. M., Viciani, S., D'Amato, F., Shur, G. N., Belyaev, G. V., Law, K. S., and Cairo, F.: In situ measurements of tropical cloud properties in the West African Monsoon: upper tropospheric ice clouds, Mesoscale Convective System outflow, and subvisual cirrus, Atmospheric Chemistry and Physics, 11, 5569–5590, http://dx.doi.org/10.5194/acp-11-5569-2011, 2011.

Goodman, J., Verma, S., Pueschel, R. F., Hamill, P., Ferry, G. V., and Webster, D.: New evidence of size and composition of polar stratospheric cloud particles, Geophysical Research Letters, 24, 615–618, http://dx.doi.org/10.1029/97GL00256, 1997.

Grooß, J.-U., Engel, I., Borrmann, S., Frey, W., Günther, G., Hoyle, C. R., Kivi, R., Luo, B. P., Molleker, S., Peter, T., Pitts, M. C., Schlager, H., Stiller, G., Vömel, H., Walker, K. A., and Müller, R.: Nitric acid trihydrate nucleation and denitrification in the Arctic stratosphere, Atmospheric Chemistry and Physics, 14, 1055–1073, http://dx.doi.org/10.5194/acp-14-1055-2014, 2014.

Hanson, D. and Mauersberger, K.: Laboratory studies of the nitric acid trihydrate: Implications for the south polar stratosphere, Geophys. Res. Lett., 15, 855–858, http://dx.doi.org/10.1029/GL015i008p00855, 1988.

Hoyle, C. R., Engel, I., Luo, B. P., Pitts, M. C., Poole, L. R., Grooß, J.-U., and Peter, T.: Heterogeneous formation of polar stratospheric clouds – Part 1: Nucleation of nitric acid trihydrate (NAT), Atmospheric Chemistry and Physics, 13, 9577–9595, http://dx.doi.org/10.5194/acp-13-9577-2013, 2013.

Kaufmann, M., Blank, J., Friedl-Vallon, F., Gerber, D., Guggenmoser, T., Höpfner, M., Kleinert, A., Sha, M. K., Oelhaf, H., Riese, M., Suminska-Ebersoldt, O., Woiwode, W., Siddans, R., Kerridge, B., Moyna, B., Rea, S., and Oldfield, M.: Technical assistance for the deployment of airborne limb sounders during ESSenCe, Technical report, ESA-ESTEC, 2013.

Kaufmann, M., Blank, J., Guggenmoser, T., Ungermann, J., Engel, A., Ern, M., Friedl-Vallon, F., Gerber, D., Grooss, J. U., Guenther, G., Höpfner, M., Kleinert, A., Latzko, T., Maucher, G.,

Neubert, T., Nordmeyer, H., Oelhaf, H., Olschewski, F., Orphal, J., Preusse, P., Schlager, H., Schneider, H., Schuettemeyer, D., Stroh, F., Suminska-Ebersoldt, O., Vogel, B., Volk, C. M., Woiwode, W., and Riese, M.: Retrieval of three-dimensional small scale structures in upper tropospheric/lower stratospheric composition as measured by GLORIA, Atmospheric Measurement Techniques Discussion, 7, 4229–4274, http://dx.doi.org/10.5194/amtd-7-4229-2014, 2014.

Korolev, A.: Reconstruction of the Sizes of Spherical Particles from Their Shadow Images. Part I: Theoretical Considerations, J. Atmos. Oceanic Technol., 24, 376–389, http://dx.doi.org/10.1175/JTECH1980.1, 2007.

Krieger, U. K., Mössinger, J. C., Luo, B., Weers, U., and Peter, T.: Measurement of the Refractive Indices of H$_2$SO$_4$-HNO$_3$-H$_2$O Solutions to Stratospheric Temperatures, Appl. Opt., 39, 3691–3703, http://dx.doi.org/10.1364/AO.39.003691, 2000.

Lance, S., Brock, C. A., Rogers, D., and Gordon, J. A.: Water droplet calibration of the Cloud Droplet Probe (CDP) and in-flight performance in liquid, ice and mixed-phase clouds during ARCPAC, Atmospheric Measurement Techniques, 3, 1683–1706, http://dx.doi.org/10.5194/amt-3-1683-2010, 2010.

Larsen, N., Knudsen, B. M., Svendsen, S. H., Deshler, T., Rosen, J. M., Kivi, R., Weisser, C., Schreiner, J., Mauerberger, K., Cairo, F., Ovarlez, J., Oelhaf, H., and Spang, R.: Formation of solid particles in synoptic-scale Arctic PSCs in early winter 2002/2003, Atmospheric Chemistry and Physics, 4, 2001–2013, http://dx.doi.org/10.5194/acp-4-2001-2004, 2004.

Lowe, D., MacKenzie, A. R., Schlager, H., Voigt, C., Dörnbrack, A., Mahoney, M. J., and Cairo, F.: Liquid particle composition and heterogeneous reactions in a mountain wave Polar Stratospheric Cloud, Atmospheric Chemistry and Physics, 6, 3611–3623, http://dx.doi.org/10.5194/acp-6-3611-2006, 2006.

Luo, B., Krieger, U. K., and Peter, T.: Densities and refractive indices of H$_2$SO$_4$/HNO$_3$/H$_2$O solutions to stratospheric temperatures, Geophys. Res. Lett., 23, 3707–3710, http://dx.doi.org/10.1029/96GL03581, 1996.

Marti, J. and Mauersberger, K.: A survey and new measurements of ice vapor pressure at temperatures between 170 and 250K, Geophys. Res. Lett., 20, 363–366, http://dx.doi.org/10.1029/93GL00105, 1993.

Middlebrook, A. M., Berland, B. S., George, S. M., Tolbert, M. A., and Toon, O. B.: Real refractive indices of infrared-characterized nitric-acid/ice films: Implications for optical measurements of polar stratospheric clouds, Journal of Geophysical Research: Atmospheres, 99, 25 655–25 666, http://dx.doi.org/10.1029/94JD02391, 1994.

Mitev, V., Matthey, R., and Makarov, V.: Miniature backscatter lidar for cloud and aerosol observation from high altitude aircraft, Recent Res. Devel. Geophysics, vol. 4, Research Signpost, 2002.

Mitev, V., Poole, L. R., Pitts, M. C., and Matthey, R.: Comparison case between CALIPSO Lidar and MALs on M55 Geophysica during RECONCILE Campaign, 26th International Laser Radar Conference, 25-29 July 2012, Porto Heli - Greece, 2012.

Müller, R. and Peter, T.: The Numerical Modelling of the Sedimentation of Polar Stratospheric Cloud Particles, Berichte der Bunsengesellschaft für physikalische Chemie, 96, 353–361, http://dx.doi.org/10.1002/bbpc.19920960323, 1992.

Northway, M. J., Gao, R. S., Popp, P. J., Holecek, J. C., Fahey, D. W., Carslaw, K. S., Tolbert, M. A., Lait, L. R., Dhaniyala, S., Flagan, R. C., Wennberg, P. O., Mahoney, M. J., Herman, R. L., Toon, G. C., and Bui, T. P.: An analysis of large HNO$_3$-containing particles sampled in the Arctic stratosphere during the winter of 1999/2000, Journal of Geophysical Research: Atmospheres, 107, SOL 41–1–SOL 41–22, http://dx.doi.org/10.1029/2001JD001079, 2002.

Peter, T.: Microphysics and Heterogeneous Chemistry of Polar Stratospheric Clouds, Annu. Rev. Phys. Chem., 48, 785–822, http://dx.doi.org/10.1146/annurev.physchem.48.1.785, 1997.

Peter, T. and Grooß, J.-U.: Stratospheric Ozone Depletion and Climate Change, Chapter 4, The Royal Society of Chemistry, pp. 108–144, http://dx.doi.org/10.1039/9781849733182, 2011.

Peter, T., Müller, R., Crutzen, P. J., and Deshler, T.: The lifetime of leewave – induced ice particles in the Arctic stratosphere: II. Stabilization due to NAT-coating, Geophysical Research Letters, 21, 1331–1334, http://dx.doi.org/10.1029/93GL03019, 1994.

Pitts, M. C., Poole, L. R., Dörnbrack, A., and Thomason, L. W.: The 2009/2010 Arctic polar stratospheric cloud season: a CALIPSO perspective, Atmospheric Chemistry and Physics, 11, 2161–2177, http://dx.doi.org/10.5194/acp-11-2161-2011, 2011.

Ramaswamy, V., Chanin, M.-L., Angell, J., Barnett, J., Gaffen, D., Gelman, M., Keckhut, P., Koshelkov, Y., Labitzke, K., Lin, J.-J. R., O'Neill, A., Nash, J., Randel, W., Rood, R., Shine, K., Shiotani, M., and Swinbank, R.: Stratospheric temperature trends: Observations and model simulations, Reviews of Geophysics, 39, 71–122, http://dx.doi.org/10.1029/1999RG000065, 2001.

Randel, W. J., Shine, K. P., Austin, J., Barnett, J., Claud, C., Gillett, N. P., Keckhut, P., Langematz, U., Lin, R., Long, C., Mears, C., Miller, A., Nash, J., Seidel, D. J., Thompson, D. W. J., Wu, F., and Yoden, S.: An update of observed stratospheric temperature trends, Journal of Geophysical Research: Atmospheres, 114, n/a–n/a, http://dx.doi.org/10.1029/2008JD010421, 2009.

Shur, G., Sitnikov, N., and Drynkov, A.: A mesoscale structure of meteorological fields in the tropopause layer and in the lower stratosphere over the southern tropics (Brazil), Russian Meteorology and Hydrology, 32, 487–494, http://dx.doi.org/10.3103/S106837390708002X, 2007.

Solomon, S.: Stratospheric ozone depletion: A review of concepts and history, Reviews of Geophysics, 37, 275–316, http://dx.doi.org/10.1029/1999RG900008, 1999.

Solomon, S., Garcia, R. R., Rowland, F. S., and Wuebbles, D. J.: On the depletion of Antarctic ozone, Nature, 321, 755–758, http://dx.doi.org/10.1038/321755a0, 1986.

Thompson, D. W. J. and Solomon, S.: Recent Stratospheric Climate Trends as Evidenced in Radiosonde Data: Global Structure and Tropospheric Linkages, J. Climate, 18, 4785–4795, http://dx.doi.org/10.1175/JCLI3585.1, 2005.

Toon, O. B., Hamill, P., Turco, R. P., and Pinto, J.: Condensation of HNO$_3$ and HCl in the winter polar stratospheres, Geophysical Research Letters, 13, 1284–1287, http://dx.doi.org/10.1029/GL013i012p01284, 1986.

Toon, O. B., Browell, E. V., Kinne, S., and Jordan, J.: An analysis of lidar observations of polar stratospheric clouds, Geophysical Research Letters, 17, 393–396, http://dx.doi.org/10.1029/GL017i004p00393, 1990.

Voigt, C., Schreiner, J., Kohlmann, A., Zink, P., Mauersberger, K., Larsen, N., Deshler, T., Kroger, C., Rosen, J., Adriani, A., Cairo, F., Donfrancesco, G. D., Viterbini, M., Ovarlez, J., Ovarlez, H., David, C., and Dörnbrack, A.: Nitric Acid Trihydrate (NAT) in

Polar Stratospheric Clouds, Science, 290, 1756–1758, http://dx.doi.org/10.1126/science.290.5497.1756, 2000.

Voigt, C., Larsen, N., Deshler, T., Kröger, C., Schreiner, J., Mauersberger, K., Luo, B., Adriani, A., Cairo, F., Di Donfrancesco, G., Ovarlez, J., Ovarlez, H., Dörnbrack, A., Knudsen, B., and Rosen, J.: In situ mountain-wave polar stratospheric cloud measurements: Implications for nitric acid trihydrate formation, J. Geophys. Res., 108, 8331, http://dx.doi.org/10.1029/2001JD001185, 2003.

Voigt, C., Schlager, H., Luo, B. P., Dörnbrack, A., Roiger, A., Stock, P., Curtius, J., Vössing, H., Borrmann, S., Davies, S., Konopka, P., Schiller, C., Shur, G., and Peter, T.: Nitric Acid Trihydrate (NAT) formation at low NAT supersaturation in Polar Stratospheric Clouds (PSCs), Atmospheric Chemistry and Physics, 5, 1371–1380, http://dx.doi.org/10.5194/acp-5-1371-2005, 2005.

von Hobe, M., Bekki, S., Borrmann, S., Cairo, F., D'Amato, F., Di Donfrancesco, G., Dörnbrack, A., Ebersoldt, A., Ebert, M., Emde, C., Engel, I., Ern, M., Frey, W., Genco, S., Griessbach, S., Grooß, J.-U., Gulde, T., Günther, G., Hösen, E., Hoffmann, L., Homonnai, V., Hoyle, C. R., Isaksen, I. S. A., Jackson, D. R., Jánosi, I. M., Jones, R. L., Kandler, K., Kalicinsky, C., Keil, A., Khaykin, S. M., Khosrawi, F., Kivi, R., Kuttippurath, J., Laube, J. C., Lefèvre, F., Lehmann, R., Ludmann, S., Luo, B. P., Marchand, M., Meyer, J., Mitev, V., Molleker, S., Müller, R., Oelhaf, H., Olschewski, F., Orsolini, Y., Peter, T., Pfeilsticker, K., Piesch, C., Pitts, M. C., Poole, L. R., Pope, F. D., Ravegnani, F., Rex, M., Riese, M., Röckmann, T., Rognerud, B., Roiger, A., Rolf, C., Santee, M. L., Scheibe, M., Schiller, C., Schlager, H., Siciliani de Cumis, M., Sitnikov, N., Søvde, O. A., Spang, R., Spelten, N., Stordal, F., Suminska-Ebersoldt, O., Ulanovski, A., Ungermann, J., Viciani, S., Volk, C. M., vom Scheidt, M., von der Gathen, P., Walker, K., Wegner, T., Weigel, R., Weinbruch, S., Wetzel, G., Wienhold, F. G., Wohltmann, I., Woiwode, W., Young, I. A. K., Yushkov, V., Zobrist, B., and Stroh, F.: Reconciliation of essential process parameters for an enhanced predictability of Arctic stratospheric ozone loss and its climate interactions (RECONCILE): activities and results, Atmospheric Chemistry and Physics, 13, 9233–9268, http://dx.doi.org/10.5194/acp-13-9233-2013, 2013.

Wagner, R., Möhler, O., Saathoff, H., Stetzer, O., and Schurath, U.: Infrared Spectrum of Nitric Acid Dihydrate: Influence of Particle Shape, The Journal of Physical Chemistry A, 109, 2572–2581, http://dx.doi.org/10.1021/jp044997u, 2005.

Waibel, A. E., Peter, T., Carslaw, K. S., Oelhaf, H., Wetzel, G., Crutzen, P. J., Pöschl, U., Tsias, A., Reimer, E., and Fischer, H.: Arctic Ozone Loss Due to Denitrification, Science, 283, 2064–2069, http://dx.doi.org/10.1126/science.283.5410.2064, 1999.

Wegner, T., Grooß, J.-U., von Hobe, M., Stroh, F., Sumińska-Ebersoldt, O., Volk, C. M., Hösen, E., Mitev, V., Shur, G., and Müller, R.: Heterogeneous chlorine activation on stratospheric aerosols and clouds in the Arctic polar vortex, Atmospheric Chemistry and Physics, 12, 11 095–11 106, http://dx.doi.org/10.5194/acp-12-11095-2012, 2012.

Weigel, R., Hermann, M., Curtius, J., Voigt, C., Walter, S., Böttger, T., Lepukhov, B., Belyaev, G., and Borrmann, S.: Experimental characterization of the COndensation PArticle counting System for high altitude aircraft-borne application, Atmospheric Measurement Techniques, 2, 243–258, http://dx.doi.org/10.5194/amt-2-243-2009, 2009.

Weisser, C., Mauersberger, K., Schreiner, J., Larsen, N., Cairo, F., Adriani, A., Ovarlez, J., and Deshler, T.: Composition analysis of liquid particles in the Arctic stratosphere under synoptic conditions, Atmospheric Chemistry and Physics, 6, 689–696, http://dx.doi.org/10.5194/acp-6-689-2006, 2006.

Wetzel, G., Oelhaf, H., Kirner, O., Friedl-Vallon, F., Ruhnke, R., Ebersoldt, A., Kleinert, A., Maucher, G., Nordmeyer, H., and Orphal, J.: Diurnal variations of reactive chlorine and nitrogen oxides observed by MIPAS-B inside the January 2010 Arctic vortex, Atmospheric Chemistry and Physics, 12, 6581–6592, http://dx.doi.org/10.5194/acp-12-6581-2012, 2012.

Woiwode, W., Oelhaf, H., Gulde, T., Piesch, C., Maucher, G., Ebersoldt, A., Keim, C., Höpfner, M., Khaykin, S., Ravegnani, F., Ulanovsky, A. E., Volk, C. M., Hösen, E., Dörnbrack, A., Ungermann, J., Kalicinsky, C., and Orphal, J.: MIPAS-STR measurements in the Arctic UTLS in winter/spring 2010: instrument characterization, retrieval and validation, Atmospheric Measurement Techniques, 5, 1205–1228, http://dx.doi.org/10.5194/amt-5-1205-2012, 2012.

Woiwode, W., Grooß, J.-U., Oelhaf, H., Molleker, S., Borrmann, S., Ebersoldt, A., Frey, W., Gulde, T., Khaykin, S., Maucher, G., Piesch, C., and Orphal, J.: Denitrification by large NAT particles: the impact of reduced settling velocities and hints on particle characteristics, Atmospheric Chemistry and Physics Discussions, 14, 5893–5927, http://dx.doi.org/10.5194/acpd-14-5893-2014, 2014.

Worsnop, D. R., Zahniser, M. S., Fox, L. E., and Wofsy, S. C.: Vapor Pressures of Solid Hydrates of Nitric Acid: Implications for Polar Stratospheric Clouds, Science, 259, 71–74, http://dx.doi.org/10.1126/science.259.5091.71, 1993.

Zöger, M., Afchine, A., Eicke, N., Gerhards, M.-T., Klein, E., McKenna, D. S., Morschel, U., Schmidt, U., Tan, V., Tuitjer, F., Woyke, T., and Schiller, C.: Fast in situ stratospheric hygrometers: A new family of balloon-borne and airborne Lyman-alpha photofragment fluorescence hygrometers, Journal of Geophysical Research: Atmospheres, 104, 1807–1816, http://dx.doi.org/10.1029/1998JD100025, 1999.
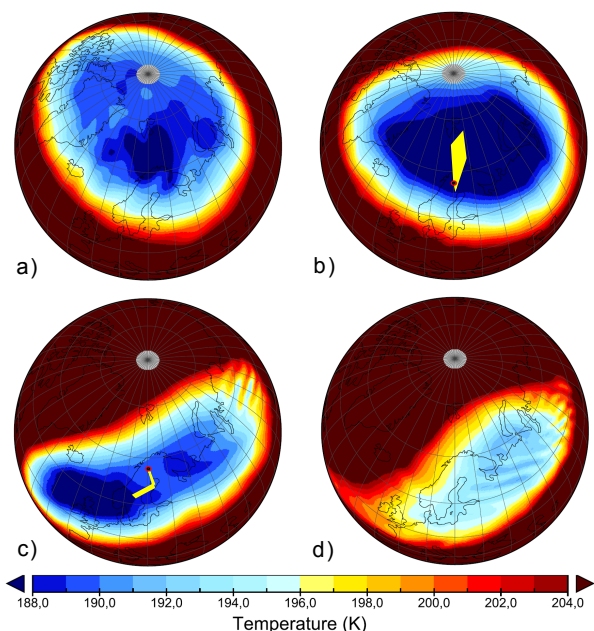
Fig. 01. ERA Interim data of temperature at the 30 hPa level during RECONCILE in January 2010: **(a)** 10 January 00:00 UTC **(b)** 17 January 12:00 UTC – corresponds to 1st PSC flight. Here the measurement region of the first four flights (17-24 January) is marked as yellow area. **(c)** 25 January 12:00 UTC – last flight with PSC occurrence as indicated with the flight track. **(d)** 28 January 18:00 UTC. The darkest blue color in the plot is scaled for temperature below 188 K to illustrate regions with temperatures close to, or below T_{ICE}.

Table 01. Numbers of particles (with size diameters Dp above the indicated values) measured by the FSSP-100 compared to the number of CIPgs images detected in PSCs. *For the flight on 20 January 2010 the data of FSSP-300 was taken and scaled to the FSSP-100's sample area.

RECONCILE flight date	number of CIPgs images	FSSP-100 Dp > 20 µm	FSSP-100 Dp > 15 µm
20 January 2010	31	5*	20*
22 January 2010	55	16	59
24 January 2010	22	3	26
25 January 2010	149	45	111
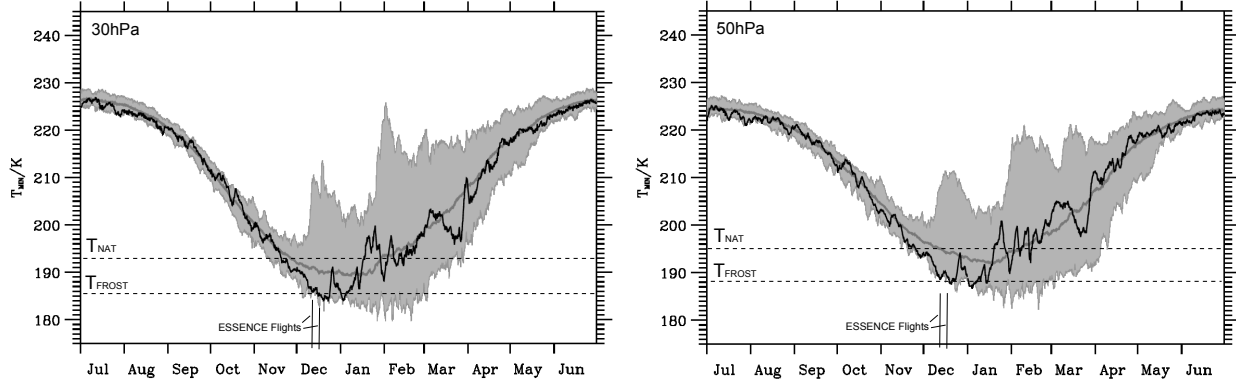
Fig. 02. Climatology of temperatures between 65° and 90° N (grey curve) and range of minimum temperatures (shaded area) in the region of Figure 1 at 30 hPa (left panel) and 50 hPa (right panel) for the years between 1989 and 2009. The black curve displays the minimum temperature for the winter 2011/2012 where two flights with M-55 were conducted. The plot is analogous to the figure provided for the winter 2009/2010 in Dörnbrack et al. (2012) with the same data source (ECMWF reanalysis at 6 hourly temporal resolutions) and PSC formation temperatures T_{NAT} and T_{ICE} calculated for 5 ppmv of water vapor and 10 ppbv of nitric acid trihydrate (NAT).
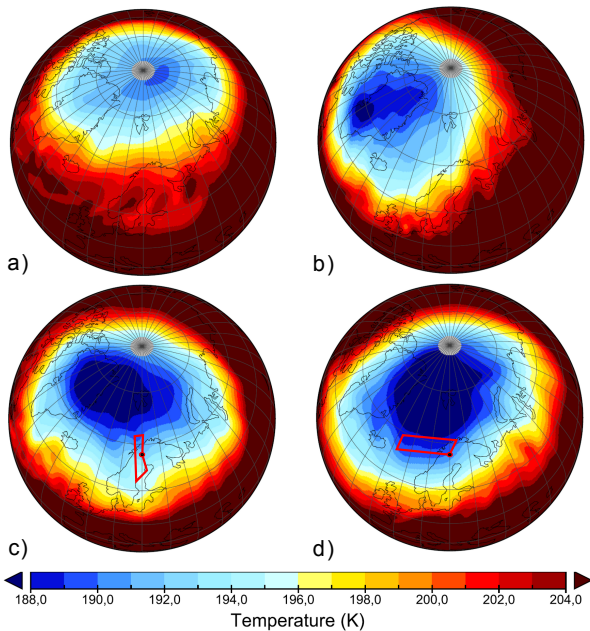
Fig. 03. ERA Interim Data of temperature at the 30 hPa level during the ESSenCe campaign on the following UTC times in December 2011: **(a)** 4 December 00:00 **(b)** 8 December 18:00 **(c)** 11 December 12:00 – corresponding to the first flight, **(d)** 6 December 18:00 – close to the second flight. Flight tracks are denoted as red lines. The polar vortex established during December 2011.
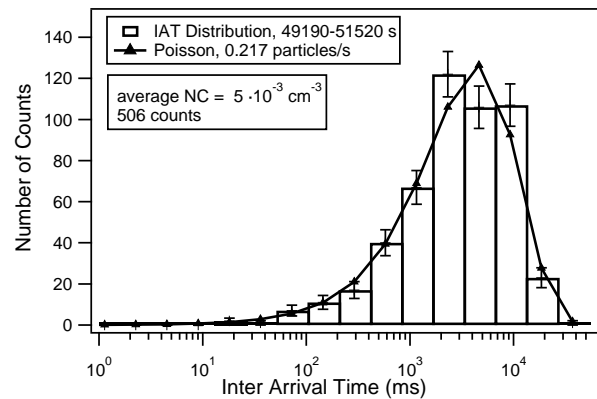
Fig. 04. The distribution of the inter arrival times (IAT) based on the CDP's particle by particle data is used to check the quality of the PSC-measurement (11 December 2011). The distribution shows inter arrival times of PSC-particles detected in about 40 min of flight time (i.e. 400 km) which is in a good agreement with the Poisson statistics (triangle marks). This implies that the detected particles were randomly distributed in a homogeneous cloud field. The CDP's (or FSSP's) counting statistics are not sufficient to resolve small spatial variations in the number density on a scale below about 200-400 km. The distribution consists of 506 particle counts with an average number concentration (NC) of $5 \cdot 10^{-3}\,\mathrm{cm}^{-3}$, which corresponds to a count rate (i.e. probability) of 0.217 particles per second. This rate and the total number of counts are the parameters of the Poisson probability distribution.
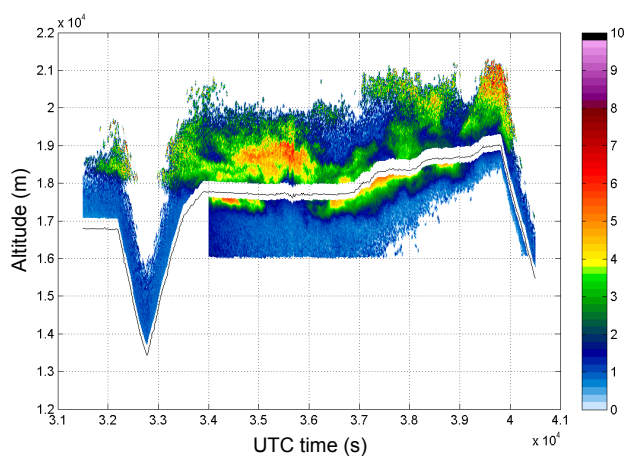
Fig. 05. Backscatter ratio profile of the up- and downward looking lidars (MAL1 and MAL2) operated onboard the M-55 *Geophysica* for the second part of the flight on 20 January 2010. A PSC field is visible along a flight leg of about 900 km length. Due to limitations in the dynamical range of the lidars, data from a distance less than 200 m to the aircraft is not recorded.
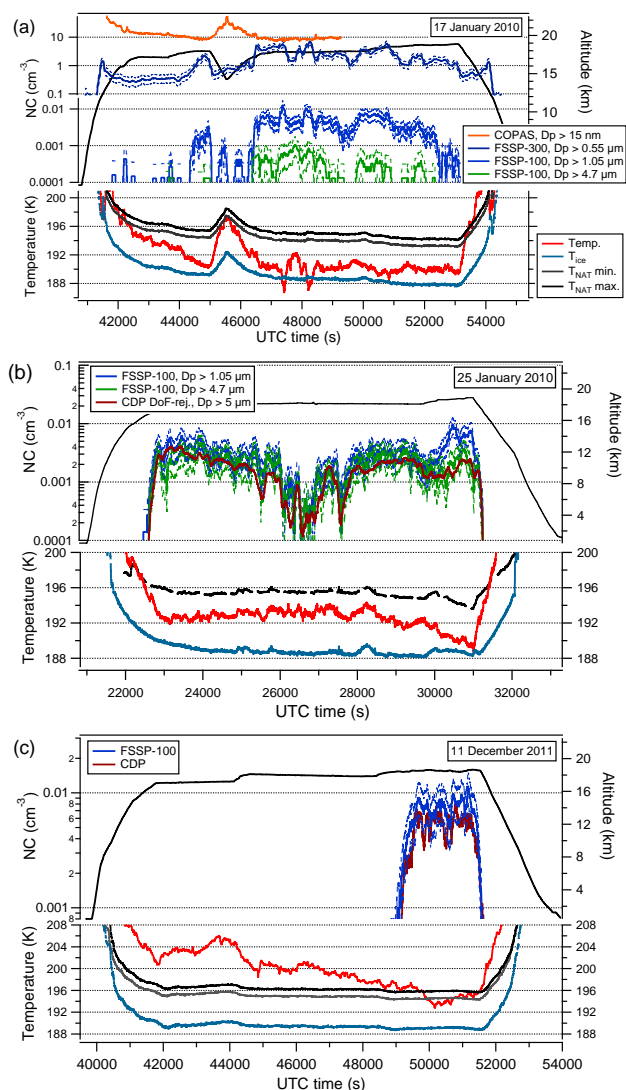

Fig. 06. Time series of the FSSP number concentrations (NC) of two RECONCILE and one ESSenCe flights overlaid with relevant temperatures: ambient temperature (red), NAT equilibrium T_{NAT} (black, grey) and frostpoint T_{ICE} (blue). T_{NAT} is estimated for 5 and 10 ppbv of HNO$_3$ where no in situ NO$_y$ data is available; otherwise in situ SIOUX-NO$_y$ data was used. Panel **(a)**: For the flight of 17 January 2010 FSSP-300-data is available and is compared to the particle number concentration measured by COPAS, with a detection limit of 15 nm. Here the synoptic scale of PSCs is apparent between 46 000 and 53 000 UT seconds. Panel **(b)**: RECONCILE-Flight on 25 January 2010. In this flight, the highest density of large (20-30 µm) HNO$_3$-containing particles of the campaign was encountered. The number concentration derived from the counting of the DoF-rejected particles (dark red curve) shows good agreement to the number concentration of the FSSP-100 for 4.7 µm cutoff (green). Note that the curve deduced from the DoF-rejected events has much better counting statistics. Panel **(c)**: ESSenCe-flight on 11 December 2011 with simultaneous measurement of the CDP and FSSP-100. Upper and lower dashed lines indicate the combined uncertainty due to the uncertainties of sample volume and counting statistics.
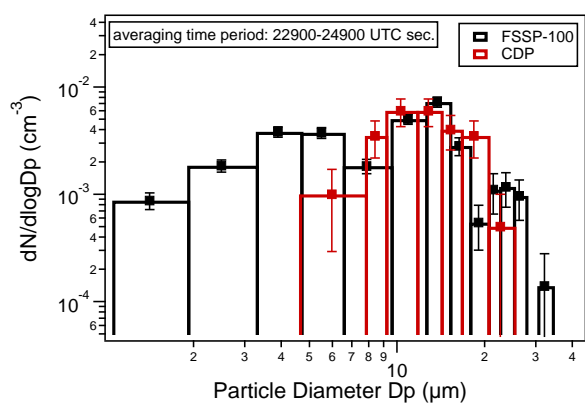
Fig. 07. PSC particle size distributions of the FSSP-100 and CDP measured on the flight of 25 January 2010. Due to instrumental problems only in this one flight of the RECONCILE-campaign the particles detection of the CDP worked well with a higher than usual detection size limit of about 5-8 μm. At the same time the largest PSC-particles in relatively high numbers were present in this flight. Note though that the FSSP-size bins above 30 μm contain only 3 counts.
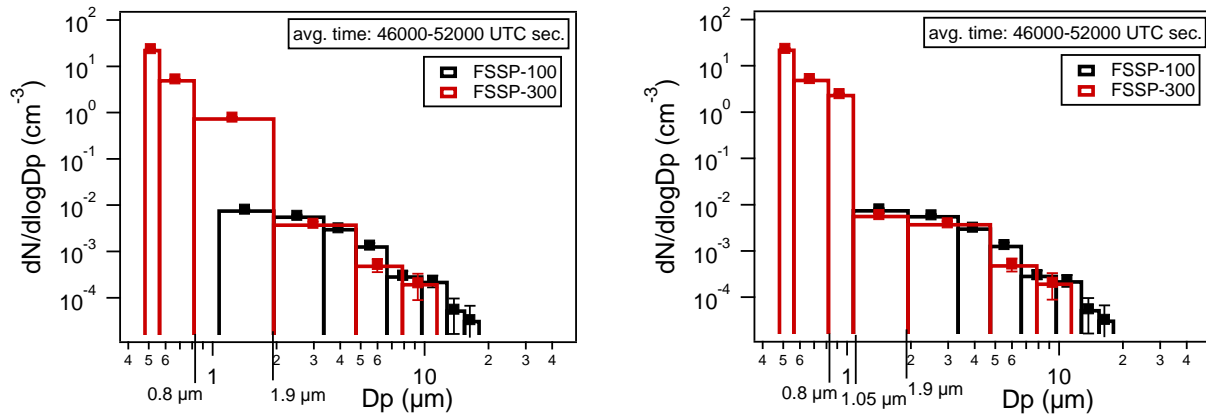
Fig. 08. Size distributions of the FSSP-100 and FSSP-300 from a PSC encounter of 1.67 hours duration are compared for the complete PSC-event during the first RECONCILE-flight (17 January 2010). The sizing of particles between about 0.8 and 1.9 µm is uncertain due to ambiguity in the Mie-calibration curve. This is taken into account by the wide size bin, which consists of several instrumental raw size bins. At the same time the detected particle numbers exhibit a decrease of about two orders of magnitude over this size range. Assuming that most of the particles belong to the STS-Mode with spherical shape and sizes closer to the lower bin limit, the discrepancy of the FSSP-100 and FSSP-300 can be explained. This is shown in the right panel, where the FSSP-300 size bin is divided by ignoring the ambiguity inherent in the Mie-curve. The initially "suspected" apparent discrepancy between the two instruments in the overlapping bin can be understood this way.
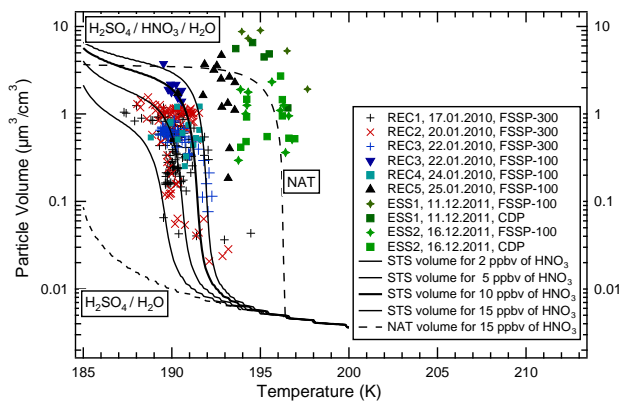

Fig. 09. Measured particle volumes vs. temperature and theoretical calculations as discussed in Peter (1997). The STS-mode size range was partly resolved by the FSSP-300. The measured data points are designated as crosses, which also indicate that only particle diameters below 2 µm were integrated for calculation of the particle volume. The theoretical curve for STS volume was calculated according to Carslaw et al. (1995) with the FSSP-300 lower cut off at 0.46 µm. Four curves for different mixing ratios of HNO$_3$ of 2, 5, 10 and 15 ppbv are plotted. Filled symbols contain only volumes including particle diameters above 2 µm. The dashed lines indicate particle volumes for the binary solution and for NAT assuming 15 ppbv of HNO$_3$.
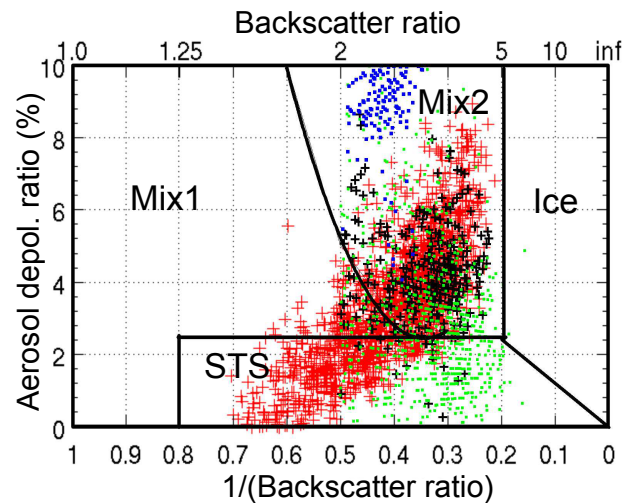

Fig. 010. Scatterplot of aerosol depolarization ratio versus backscatter ratio as measured by the lidars MAL1 and MAL2 (red crosses) on 20 January (see Figure 05), and near in situ by the backscattersonde MAS, on 17 January 2010 (green squares), 20 January (black crosses), 25 January (blue squares). The black lines are phase boundaries for different (lidar) PSC types adopted from the scheme described in Pitts et al. (2011). Mix 1 and Mix 2 are mixtures of liquid droplets and solid NAT particles defined for different number densities of NAT particles. Mix 2 represents NAT number densities above 10^{-3} cm^{-3}.
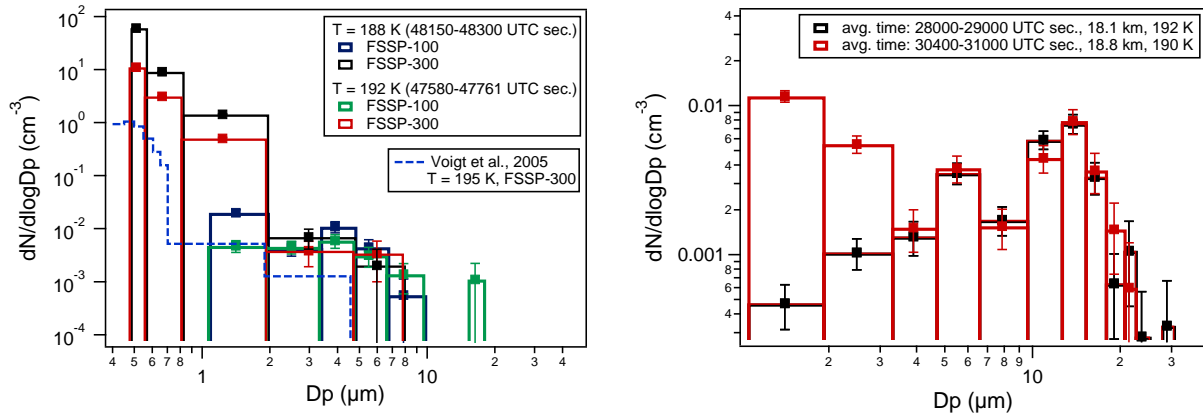
Fig. 011. Size distributions of synoptic scale Arctic PSCs as taken from successive time intervals within same flight (left panel: 17 January 2010 and right panel: 25 January 2010) but with different temperatures and altitudes. In the left panel, for comparison a FSSP-300 size distribution from a lee wave PSC (Voigt et al., 2005) is integrated, where atmospheric conditions of heterogeneous NAT nucleation without the preexistence of ice particles were encountered. The counting statistics is such that no error bars are visible in the graph for the smallest particles. These two figures show the NAT rock mode and the STS mode as distinguishably separate modes. On the right panel the NAT size range may contain an additional, separate particle mode at size diameters Dp between about 5 to 6 μm.
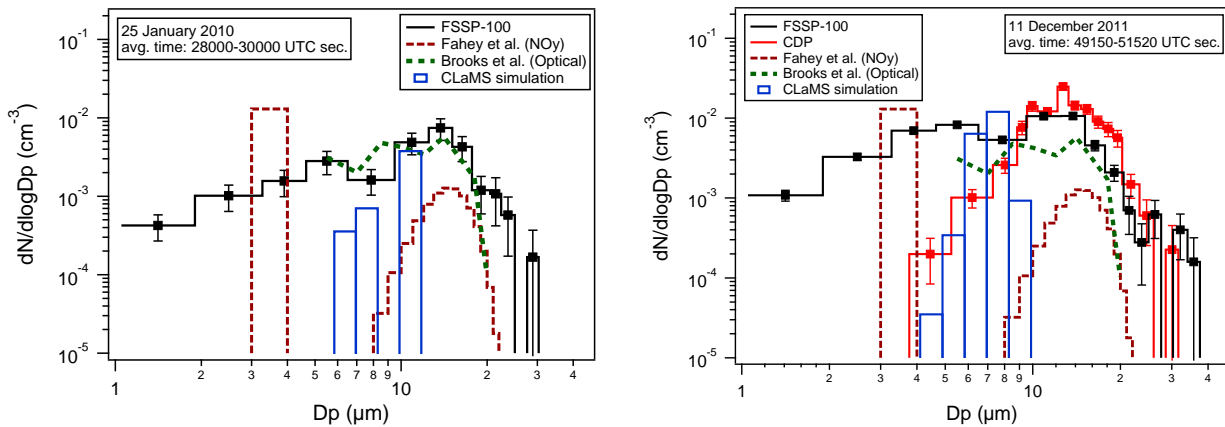

Fig. 012. Size distributions of large HNO$_3$-containing PSC particles with the highest number densities from the 2010 and 2011 campaigns. The RECONCILE flight on 25 January 2010 is shown on the left panel, the ESSenCe flight on 11 December 2011 on the right - where the number density and particle volume is about a factor of 2 higher compared with the largest values from RECONCILE. CLaMS model simulations (blue) for the corresponding coordinates of space and time do not reproduce NAT particle diameters above 12 μm. Both measurements are compared to similar findings in Fahey et al. 2001 (retrieved from total NO$_y$) and Brooks et al. 2003 (optical measurements).
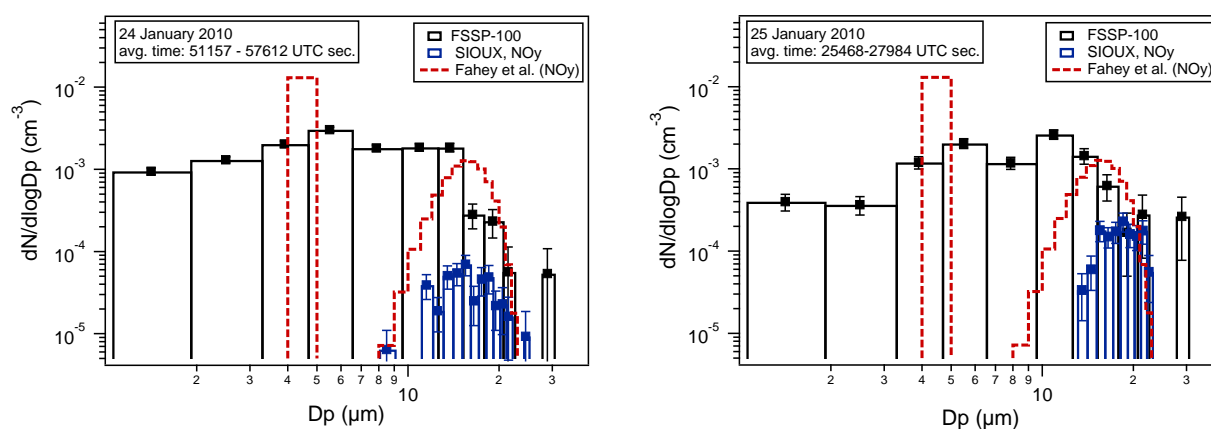
Fig. 013. PSC particle size distributions of the FSSP-100 data for time intervals where the total NO$_y$ data of the SIOUX instruments allowed extraction of particle data from single peaks, and for which diameters assuming NAT composition were derived. The sensitivity of the NO$_y$ instrument scales with particle volume, so that sizes only above about 10 μm could be retrieved. A particle size independent enhancement factor was used, which might explain some of the discrepancy in the particle numbers between the NO$_y$ and the optical measurements.
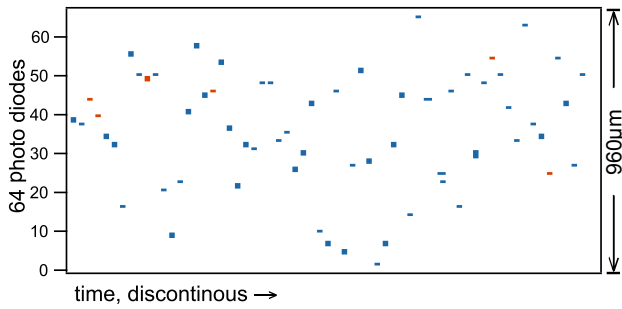
Fig. 014. Example of the 62 CIP grey scale single cloud particle images, shown here as square blue or red elements, recorded over about 30 minutes during a flight on 25 January 2010 in the PSC field where FSSP-100 detected significant numbers of particles larger than 10 μm (see also Table 01). The pixel size of the CIPgs (i.e. the object-distance of photo diodes on the array) is 15 μm. Most of the pixels where triggered by the first shadow threshold at 35 % (blue color). The second threshold at 50 % (red) accounts only for less than a tenth of detected events. These image-blotches can be considered as visual proof for the existence of NAT-rock sized PSC particles.
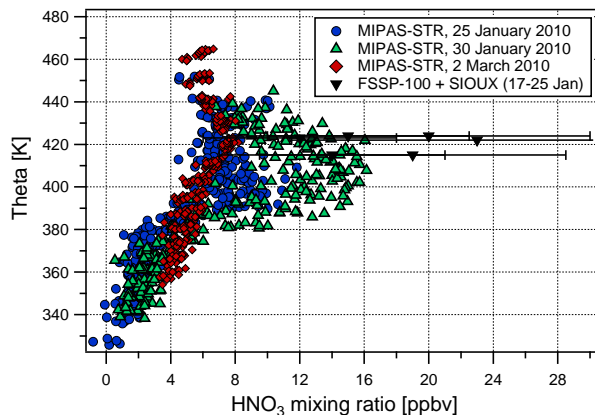

Fig. 015. Gas-phase HNO$_3$ mixing ratios retrieved from MIPAS-STR observations (also operated on board the M-55 *Geophysica*) vs. potential temperature. Enhanced HNO$_3$ mixing ratios are observed between 380 and 440 Kelvin as a result of renitrification. The most prominent renitrification signal is found for 30 January 2010 (green) (i.e. just after the PSC season as evident from Figure 2) with about 9 ppbv excess of HNO$_3$. Total HNO$_3$ mixing ratios (condensed plus gas-phase) derived from the FSSP-100 measurements together with measured SIOUX in situ gas-phase HNO$_3$ partly lie within the range of MIPAS-STR and partly exceed these values. (In the case of no available SIOUX data lower and upper limits of 2 to 7 ppbv were used.) The error bars for the FSSP+SIOUX derived mixing ratios are estimated at 50 %.